catalysts

MDPI

Article

Hydride Generation on the Cu-Doped $CeO_2(111)$ Surface and Its Role in CO_2 Hydrogenation Reactions

Zhi-Qiang Wang [1,†], Hui-Hui Liu [1,†], Xin-Ping Wu [1,*], Peijun Hu [1,2] and Xue-Qing Gong [1,*]

[1] Key Laboratory for Advanced Materials and Joint International Research Laboratory for Precision Chemistry and Molecular Engineering, Feringa Nobel Prize Scientist Joint Research Center, Centre for Computational Chemistry and Research Institute of Industrial Catalysis, School of Chemistry and Molecular Engineering, East China University of Science and Technology, 130 Meilong Road, Shanghai 200237, China
[2] School of Chemistry and Chemical Engineering, The Queen's University of Belfast, Belfast BT9 5AG, UK
* Correspondence: xpwu@ecust.edu.cn (X.-P.W.); xgong@ecust.edu.cn (X.-Q.G.)
† These authors contributed equally to this work.

Abstract: Ceria-based catalysts exhibit great activity in catalyzing selective hydrogenation of CO_2 to methanol. However, the underlying mechanism of this reaction, especially the generation of active H species, remains unclear. In this work, we performed extensive density functional theory calculations corrected by on-site Coulomb interaction (DFT + U) to investigate the H_2 dissociation and the reaction between the active H species and CO_2 on the pristine and Cu-doped $CeO_2(111)$ (denoted as $Cu/CeO_2(111)$) surfaces. Our calculations evidenced that the heterolytic H_2 dissociation for hydride generation can more readily occur on the $Cu/CeO_2(111)$ surface than on the pristine $CeO_2(111)$ surface. We also found that the Cu dopant can facilitate the formation of surface oxygen vacancies, further promoting the generation of hydride species. Moreover, the adsorption of CO_2 and the hydrogenation of CO_2 to HCOO* can be greatly promoted on the $Cu/CeO_2(111)$ surface with hydride species, which can lead to the high activity and selectivity toward CO_2 hydrogenation to methanol.

Keywords: ceria; hydride; CO_2 hydrogenation; single Cu doping; density functional theory

Citation: Wang, Z.-Q.; Liu, H.-H.; Wu, X.-P.; Hu, P.; Gong, X.-Q. Hydride Generation on the Cu-Doped $CeO_2(111)$ Surface and Its Role in CO_2 Hydrogenation Reactions. *Catalysts* **2022**, *12*, 963. https://doi.org/10.3390/catal12090963

Academic Editor: Albert Poater

Received: 14 July 2022
Accepted: 26 August 2022
Published: 29 August 2022

1. Introduction

Oxide-based materials are increasingly recognized as highly efficient and selective catalysts for hydrogenation reactions [1–6]. Among numerous metal oxides, ceria (CeO_2), which usually contains abundant oxygen vacancies (O_V) on the surface and in the bulk, has attracted great attention for its excellent performance in catalyzing reactions such as hydrogenation of CO_2 to methanol [7–12]. The combined experimental and density functional theory (DFT) study of Liu et al. [9] reported that the morphology control of CeO_2 nano-catalysts is important for methanol synthesis. They also proposed that methanol was likely generated via the so-called formate (HCOO) pathway where the adsorbed CO_2 is firstly hydrogenated to the HCOO* species. Cheng et al. [10] investigated the conversion of CO_2 to methanol on the reduced $CeO_2(110)$ surface by performing DFT calculations corrected by on-site Coulomb interaction (DFT + U) and microkinetic analysis. They also found that the HCOO route is the dominant pathway for methanol formation on the reduced $CeO_2(110)$. Kumari et al. [11] performed DFT calculations to study the mechanisms of CO_2 reduction to CO and the hydrogenation of CO_2 to methanol on both the stoichiometric and reduced $CeO_2(110)$ surfaces. It was found that CO_2 dissociates to CO through the interaction with the oxygen vacancy on the reduced ceria surface, and the produced CO can be further hydrogenated to methanol. Li et al. [12] investigated the mechanism of thermal catalytic hydrogenation of CO_2 to methanol on the reduced $CeO_2(100)$ by using DFT calculations, and they found that CO_2 was hydrogenated via

the HCOO route rather than the COOH route. These results then indicate that oxygen vacancies on the reduced CeO_2 surface are crucial to the conversion of CO_2 to CH_3OH.

Cu-based catalysts are particularly active for CO_2 hydrogenation and have been commercially utilized for CO/CO_2 hydrogenation to methanol [13–16]. Xu et al. [17,18] reported the synergetic effect of Cu and ZnO on the catalytic activity and selectivity in the direct hydrogenation of CO_2 to C_{2+} alcohols. This synergetic effect can regulate the CO_2 and H_2 activation processes to achieve the optimal concentrations of surface CH_x*, CO* and H* species for C_{2+} alcohols synthesis via CH_x*−CO* coupling and hydrogenation reactions. Jia et al. [19] found that abundant surface oxygen vacancies were in situ generated and consumed during the CO_2 reduction reaction on the Cu/CeO_2 catalyst with a Cu loading of 15 wt.%, and such vacancy sites can be combined with the adjacent copper clusters to promote the activation of CO_2 and increase the catalytic efficiency. Wang et al. [20] proposed that sub-nano Cu cubes supported on the thermally reduced CeO_2 nanorods through strong metal-support interaction (SMSI) can significantly enhance the formation and activity of hydrides species on both Cu and ceria, as compared with the Cu nanoparticles supported at stoichiometric CeO_2 nanorods. Xia et al. [21] performed DFT calculations and illustrated that the formation of oxygen vacancies was suppressed at the interface of the Cu cluster and $CeO_2(111)$, while H_2 oxidation can be facilitated and the catalytic activity can be enhanced, in comparison with the pristine $CeO_2(111)$. At the same time, single-atom catalysts were often reported to have catalytic properties that surpass those of nanoparticles [22,23]. Huang et al. [24] demonstrated that the C_3N_4-supported Cu single-atom catalysts with tailored coordination structures can serve as highly active and selective catalysts for CO_2 hydrogenation to methanol at low temperature, though the role of the Cu single atom in such catalytic process is still vague.

The study of the interaction between H_2 and ceria is crucial to understanding the mechanism of ceria catalyzed selective hydrogenation reactions [25–29]. Many studies have found that the homolytic dissociation of H_2 to form two hydroxyl (OH) groups is thermodynamically favored on the stoichiometric surface of ceria [6,30]. On the other hand, a few recent studies suggested that oxygen vacancies can facilitate the formation of active hydrides (H^-) species through heterolytic dissociation of H_2 on the reduced surface of ceria [6,31–37]. This agrees with the previous studies that reduced ceria surface is more active than the stochiometric one in CO_2 hydrogenation reactions [10,11]. Moreover, our recent studies proposed that low-coordinated Ce sites can promote the formation of H^- species even on the stoichiometric CeO_2 stepped surfaces [38], which is consistent with the finding by García-Melchor et al. [27], and suggests that oxygen vacancy may not be essential for the formation of hydrides on the CeO_2 surfaces. To better drive the hydrogenation reactions such as the CO_2 reduction reaction (CO_2-RR) under moderate conditions, the activity and stability of the hydride species would need to be further enhanced on the surfaces of the ceria-based catalysts.

In this work, we investigated the role of the Cu dopant on the $CeO_2(111)$ surface in the catalytic dissociation of H_2 to produce hydride species. Specifically, DFT + U calculations have been performed to illustrate the reactivity of H_2 dissociation on the pristine and Cu-doped $CeO_2(111)$ (denoted as $Cu/CeO_2(111)$) surfaces. Our results showed that the doping of a single Cu atom is accompanied by the formation of an oxygen vacancy on the $CeO_2(111)$ surface, and the formed oxygen vacancy can play a key role in the formation of H^- species through heterolytic H_2 dissociation. In addition, the single Cu site can also enhance the adsorption of CO_2, which is favorable for improving the catalytic activity. Our calculations further indicated that the $Cu/CeO_2(111)$ surface with H^- species exhibits high activity and selectivity in the hydrogenation of CO_2 to methanol.

2. Calculation Methods

In this work, all spin-polarized DFT calculations were carried out using the Vienna Ab–initio Simulation Package (VASP) [39]. The projector augmented wave (PAW) method [40] and the Perdew−Burke−Ernzerhof (PBE) [41] functional under the generalized gradient

approximation (GGA) [42] were applied in the calculations. The kinetic energy cut-off was set as 400 eV (Table S1), and the force threshold for structure optimizations was 0.05 eV/Å. A large vacuum gap of 15 Å was used to eliminate the interaction between neighboring slabs. Different *k*-point meshes have been tested during the optimization of the unit cell of bulk ceria. It was shown that the *k*-point mesh of (5 × 5 × 5) can give the converged result (Table S2), and the calculated lattice parameter (a = b = c = 5.456 Å) is in good agreement with the experimental value (5.411 Å), which was then used for the subsequent study [43].

We then built a *p*(3 × 3) surface slab containing three O−Ce−O layers to model the CeO_2(111) surface. To model the Cu-doped CeO_2(111), one surface Ce atom was replaced by a Cu atom and one surface oxygen nearby was removed accordingly to ensure charge conservation. The top two layers of the slabs were allowed to fully relax, while the bottom layer was kept fixed to mimic the bulk region. Due to the relatively large surface cell (11.56 Å × 11.56 Å), the *k*-point mesh of (2 × 2 × 1) suggested by previous studies was used for Brillouin-zone integrations [44]. Note that the on-site Coulomb interaction correction is necessary for the appropriate description of the localized Ce 4*f* electrons [45–47], and therefore we used an effective U value of 5 eV, as suggested by previous studies [45,46].

The transition states (TSs) of surface reactions were located using a constrained optimization scheme and were verified when (i) all forces on the relaxed atoms vanish and (ii) the total energy is a maximum along the reaction coordination but a minimum with respect to the rest of the degrees of freedom [48–50]. For example, when using this approach to calculate the transition states of H_2 dissociation, we fixed the H-H distance at preselected values and then optimized the whole system with respect to all the remaining degrees of freedom.

The adsorption energy of species X on the surface, $E_{ads}(X)$, was calculated with

$$E_{ads}(X) = -(E_{X/slab} - E_{slab} - E_X) \quad (1)$$

where $E_{X/slab}$ is the calculated total energy of the adsorption system, while E_{slab} and E_X are the calculated energies of the clean surface and the gas phase molecule X, respectively. Accordingly, a positive $E_{ads}(X)$ value indicates an energetically favorable adsorption process, and the more positive the $E_{ads}(X)$ is, the more strongly the adsorbate X binds to the surface, and this definition was also proposed by Somorjai and Li [51].

The neutral oxygen vacancy formation energy (E_{OV}) was calculated according to

$$E_{OV} = E_{slab\text{-}vac} + 1/2E_{O2} - E_{slab} \quad (2)$$

where $E_{slab\text{-}vac}$ is the total energy of the surface with a neutral oxygen vacancy and E_{O2} is the energy of a gas-phase O_2 molecule.

3. Results and Discussion

3.1. Structural and Electronic Properties

The CeO_2(111) surface is known as the most stable termination of ceria [26,27]. From Figure 1a, one can see that there are two types of lattice oxygen on the CeO_2(111) surface, namely, the three-fold coordinated O (denoted as O_{3c}) on the top layer and four-fold coordinated O (denoted as O_{4c}) on the subsurface. The calculated bond lengths of Ce−O_{3c} (2.36 Å) and Ce−O_{4c} (2.37 Å) are nearly identical. Figure 1b shows the optimized structure of the Cu-doped CeO_2(111) (Cu/CeO_2(111)). As we have explained, the doping of one Cu atom onto the CeO_2(111) surface is accompanied by the spontaneous formation of an oxygen vacancy (E_{OV} = −0.94 eV) to ensure charge conservation [52,53]. The calculated bond lengths of Ce−O_{3c} (2.35 Å) and Ce−O_{4c} (2.36 Å) on the doped Cu/CeO_2(111) are nearly identical to those of the pristine CeO_2(111). Moreover, the calculated bond lengths of Cu−O_{3c} and Cu−O_{4c} on the Cu/CeO_2(111) surface are 3.13 and 1.96 Å, respectively, and these results are consistent with previous studies [52–54]. The elongation of the Cu−O_{3c} bond also indicates that the top surface O atoms bonding to Cu are activated.

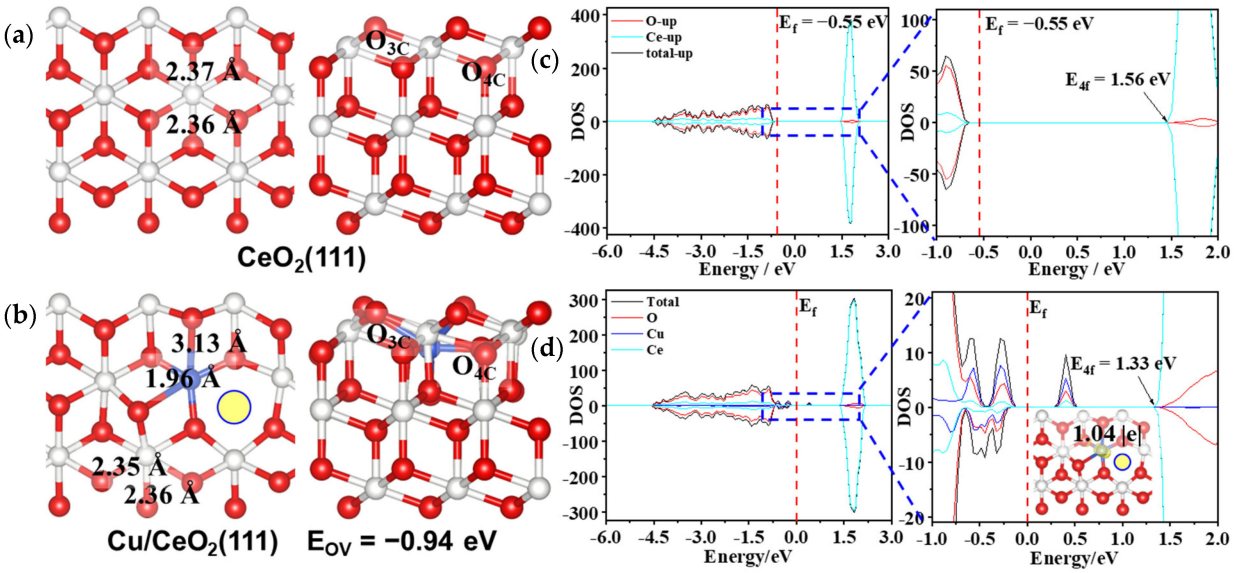

Figure 1. Calculated structures (left: top view; right: side view) of the (**a**) $CeO_2(111)$ and (**b**) $Cu/CeO_2(111)$ surfaces, and calculated density of states (DOS) of the (**c**) $CeO_2(111)$ and (**d**) $Cu/CeO_2(111)$ surfaces. The blue circles filled with yellow represent the inherent surface oxygen vacancy on the $Cu/CeO_2(111)$. Red: O atoms; ivory: Ce atoms; blue: Cu atoms. These notations are used throughout the paper. All DOS were aligned with respect to the O 2*s* orbital of a fixed bottom O atom of the surface slabs.

To better understand the doped $Cu/CeO_2(111)$, we first calculated the density of states (DOS) and spin density distribution of this surface (Figure 1d). The lowest unoccupied states are mainly composed of Cu 3*d* and O 2*p*. This indicates that the local CuO structure is capable of receiving extra electrons and may act as the catalytically active site. The calculated Bader charge of the Cu dopant is +1.04 |e|, which is close to that of the Cu^{2+} on the CuO surface (+0.97 |e|, see Table S3), indicating that the oxidation state of the Cu dopant on the $CeO_2(111)$ is indeed +2 [52,55]. This is also consistent with the calculated spin density distribution on the Cu site (Figure 1d). In addition, we also found that after Cu doping the energy level of the lowest unoccupied Ce 4*f* orbital decreases by 0.23 eV from 1.56 eV to 1.33 eV (Figure 1c,d), indicating that the electron accepting capacity of Ce 4*f* is also enhanced accordingly.

3.2. H Adsorption

Previous studies suggested that hydride is the key species for selective hydrogenation of CO_2 over ceria surfaces [10,11]. To verify the nature of various H species including proton, hydride and hydrogen radical (H•), one needs to calculate their Bader charges as well as the spin density distributions. For the hydride species, there is no (net) spin density localized on it, and the calculated Bader charges are usually negative, while for the hydrogen radical, there are spin densities localized on it and the calculated Bader charge is usually close to 0 |e|. Bearing the above in mind, we thus studied the adsorption of one H atom at different sites on the $Cu/CeO_2(111)$ surface. The calculated results show that two types of H species can be formed after H adsorption at the Cu site (Figure 2a,b). Electronic structure analyses confirmed that one adsorbed H species is a radical-like species since it has net spin densities (Figure 2a), and the other one has a Bader charge that is close to zero (Figure 2b). For the calculated adsorption energies, they are negative for both cases, though the second type gives higher value (−1.61 vs. −0.45 eV, Figure 2a,b). Moreover, the calculated density of states of the system shown in Figure S1 also indicates that a relatively stronger Cu-H bond is formed for the second adsorption structure (Figure 2b) [53,54]. In addition, we also investigated H adsorption at the surface O site. In this case, a proton (H^+)

is formed, and the surface is clearly reduced, with either the Cu or Ce taking the electron from the H (Figure 2c,d). However, it needs to be mentioned that for the reduction of Cu^{2+} to Cu^{1+} (Bader charge = 0.66 |e|), the corresponding adsorption process is exothermic by 1.99 eV (Figure 2c), and for the reduction of Ce^{4+} to Ce^{3+}, it is exothermic by 2.36 eV (Figure 2d).

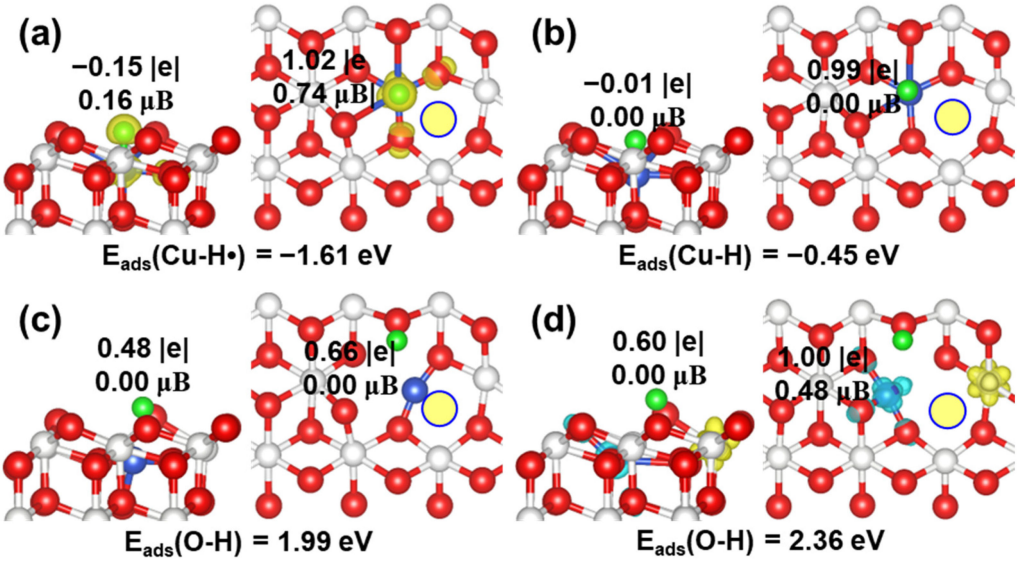

Figure 2. Calculated structures (left: side view; right: top view) of H adsorption at (**a**,**b**) Cu and (**c**,**d**) O sites of the $Cu/CeO_2(111)$ surface. The calculated adsorption energies of H, Bader charges and the magnetic moments of H (left) and Cu (right), and spin density distributions (in yellow) are also shown.

Hermansson and Fernandez-Gacia and their co-workers [52,55] have shown that the four coordinated planar Cu^{2+} is relatively stable within the $Cu/CeO_2(111)$ structure. It is interesting for us to find that with the hydrogen species being adsorbed at the O site on the $Cu/CeO_2(111)$ surface, the coordinate number of Cu maintains four when the extra electron is localized at the Ce site. On the other hand, when the extra electron is localized at the Cu, it induces the change of the coordinate number of Cu to three (Figure S2 and Table S4). In fact, we have also estimated and compared the electrostatic interaction energies at such Ce^{3+} and Cu^{1+} sites, which are −134.05 eV and −130.40 eV, respectively (see Figure S2 and Table S4). These results clearly show that the $Cu/CeO_2(111)$ surface can be more stable with the extra electron being localized at the Ce site than the Cu due to the more favorable electrostatic interaction. Moreover, the calculated density of states of the corresponding systems further showed that the newly occupied Cu 3*d* orbital is 0.15 eV higher in energy than the occupied Ce 4*f* orbital (Figure S3). These results can indeed support that the excess electron prefers to be localized in the Ce 4*f*, even though the empty Cu(3*d*)-O(2*p*) state is lower (Figure 1d).

3.3. H_2 Dissociation and H^- Formation

Recent studies have shown that ceria has the capability of catalyzing partial hydrogenation of alkynes and CO_2 reduction reactions [2,4,10,11]. The formation of hydride through heterolytic dissociation of H_2 on the CeO_2 surface was found to be one of the vital processes in these reactions [7–12,38]. Then, we systematically studied the dissociative adsorption of H_2 on both the pristine and Cu-doped $CeO_2(111)$ surfaces.

The calculated energy profiles of H_2 adsorption and dissociation on the $CeO_2(111)$ and $Cu/CeO_2(111)$ surfaces are shown in Figure 3. As one can see, the adsorption energy of H_2 on the $Cu/CeO_2(111)$ surface (0.30 eV) is 0.26 eV higher than that on the pristine $CeO_2(111)$ surface (0.04 eV), indicating that the H_2 molecule has a stronger interaction with the $Cu/CeO_2(111)$ surface. We further considered the homolytic and heterolytic

pathways of H_2 dissociation on the $CeO_2(111)$ and $Cu/CeO_2(111)$ surfaces. The homolytic dissociation produces two surface hydroxyls, while the heterolytic dissociation produces a surface hydroxyl and a hydride species [27,38]. According to our calculations, the homolytic dissociation of H_2 on the $CeO_2(111)$ (gray dotted line) and $Cu/CeO_2(111)$ surfaces (black dotted line) needs to overcome the energy barriers of 1.34 and 1.08 eV, respectively (see Figures 3, S4 and S5). In each transition state of the homolytic H_2 dissociation, one OH species and one hydrogen radical are formed on the surface firstly (Figures S4b and S5b), giving rise to rather high barrier for this process. The as-formed H radical will then migrate to the neighboring O site to form the second OH species. Moreover, on the $CeO_2(111)$ and $Cu/CeO_2(111)$ surfaces, the homolytic H_2 dissociation process was calculated to be exothermic by 2.41 and 3.25 eV, respectively.

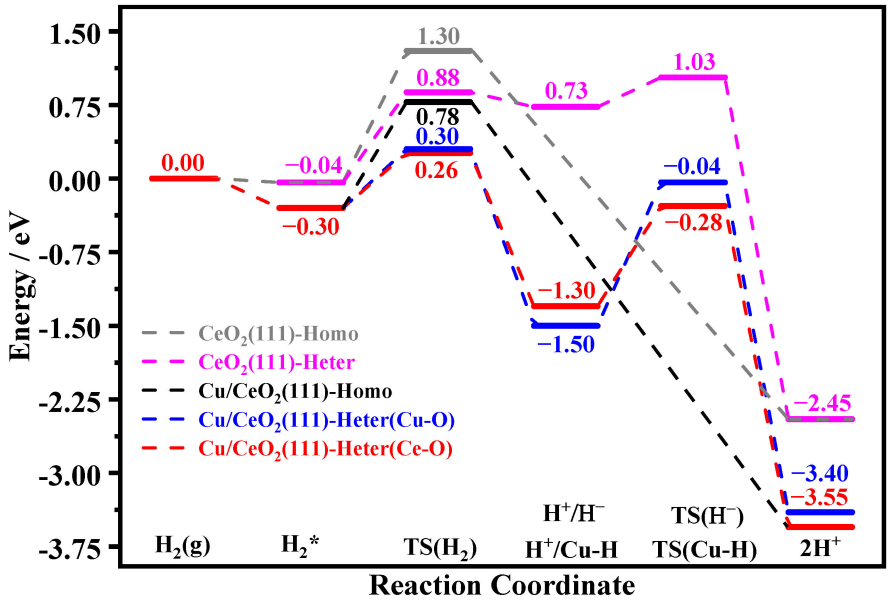

Figure 3. Calculated energy profiles of homolytic (Homo) and heterolytic (Heter) H_2 dissociation on the $CeO_2(111)$ and $Cu/CeO_2(111)$ surfaces. "*" is defined as the surface free site, and this notation is used throughout the paper.

Interestingly, our calculated results (Figures 3, S4 and S5) showed that the energy barrier for the heterolytic dissociation of H_2 at the Ce-O site on the $Cu/CeO_2(111)$ (red dotted line, 0.56 eV) is lower than that on the pristine $CeO_2(111)$ (pink dotted line, 0.92 eV) and they are both significantly lower than those of the homolytic dissociation. Following the transition state (Figures S4c and S5c), one OH and one hydride species are formed, and this process is endothermic by 0.77 eV at $CeO_2(111)$ and exothermic by 1 eV at $Cu/CeO_2(111)$. Notably, we found that the obvious stability of H^- species on the $Cu/CeO_2(111)$ surface (Figure S5d) can be attributed to the low coordination number of Ce at the oxygen vacancy. These results clearly indicate that the Cu doping promotes the formation of oxygen vacancies, which is critical for the stabilization of hydride species. We also calculated the heterolytic dissociation of H_2 at the Cu-O site on the $Cu/CeO_2(111)$ surface to produce H^+ and Cu-H species (blue dotted line). This process needs to overcome a barrier of 0.60 eV and is exothermic by 1.20 eV.

Furthermore, we also considered the migration of hydride species to the neighboring O site to form another hydroxyl species on the two surfaces. The calculated energy barriers of the migration process on the $CeO_2(111)$ and $Cu/CeO_2(111)$ surfaces are 0.30 and 1.02 eV, respectively. The high energy barrier of the migration on the $Cu/CeO_2(111)$ surface indicates that the hydride species can be kinetically stable on this surface. In addition, we calculated the migration of the hydrogen species (Cu-H) to the neighboring O site to form

another hydroxyl species on the $Cu/CeO_2(111)$ surface, and it needs to overcome an energy barrier of 1.46 eV and is exothermic by 1.90 eV (Figure 3).

It should be noted that the CeO_2 surface accepts two extra electrons after the hydride migration. For the $Cu/CeO_2(111)$, we found that the two electrons prefer to be localized in the 4*f* orbitals of two Ce atoms rather than in one Ce 4*f* orbital and one Cu 3*d* orbital as the former case is 0.15 eV more stable than the latter one (Figure S5h,j). This again indicates the significant role of Ce 4*f* as the "electron reservoir" [56].

To gain deeper insights into the effect of Cu doping on the formation of hydride species on the $Cu/CeO_2(111)$ surface, we calculated the partial density of states of the Ce^{3+} species on the two CeO_2 surfaces with one H being adsorbed at the O site. Note that this H can be regarded as the "co-adsorbate" of the other H in dissociative H_2 adsorption (Figure 4). The calculated results show that the occupied 4*f* state of the $Cu/CeO_2(111)$ with one hydroxyl lies in the higher energy than that of the $CeO_2(111)$ with one hydroxyl. So, one may expect that the Ce^{3+} species on the $Cu/CeO_2(111)$ with one hydroxyl can donate this electron to the second H to form a hydride species more readily than the Ce^{3+} species on the $CeO_2(111)$ with one hydroxyl.

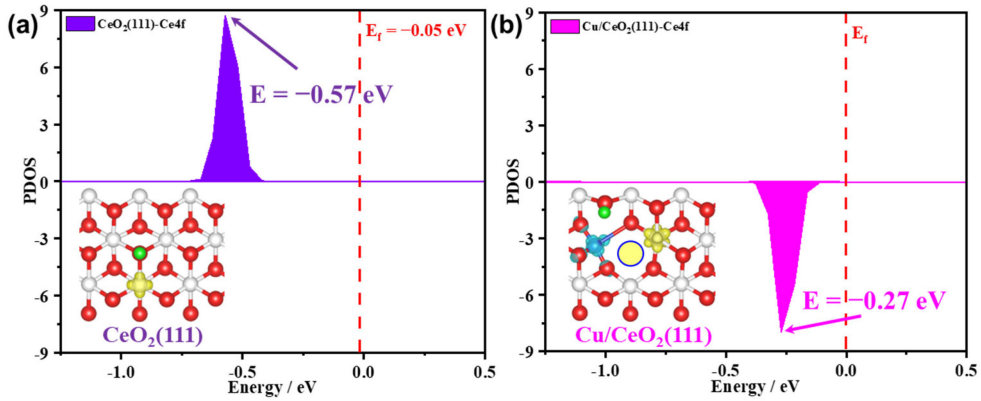

Figure 4. Calculated partial density of states (PDOS) of the Ce^{3+} on the (**a**) $CeO_2(111)$ and (**b**) $Cu/CeO_2(111)$ surfaces with one H being adsorbed on O. The Fermi energy level (E_f) is labeled with a red dashed line. All DOS are aligned with respect to the O 2*s* orbital of a fixed bottom O atom of the surface slabs.

Previous studies reported that surface oxygen vacancies can stabilize hydride species [33,37,38]. We then calculated the formation of an extra surface oxygen vacancy on the $CeO_2(111)$ and $Cu/CeO_2(111)$ (Figure 5). It was found that the $Cu/CeO_2(111)$ gives a much smaller surface oxygen vacancy formation energy (0.59 eV) than the $CeO_2(111)$ surface (2.41 eV), suggesting that the Cu dopant can further promote the formation of the surface oxygen vacancy. The newly formed surface oxygen vacancy can reduce two Ce^{4+} into Ce^{3+} cations. This is mainly due to the fact that the calculated crystal reduction potential (V_r) [57] for $Cu^{2+} \rightarrow Cu^{+}$ (−1.43 V) is higher than that for $Ce^{4+} \rightarrow Ce^{3+}$ (−1.77 V), and the coordination number of Ce around the new O_V site is also reduced (Figure 5b). We also found that it is more favorable to form hydride species on such reduced $Cu/CeO_2(111)$ surface (i.e., $Cu/CeO_2(111)$-O_V) than the $Cu/CeO_2(111)$ surface (Figure 5c,d). We calculated the dissociation of H_2 on the $Cu/CeO_2(111)$-O_V surface (Figures 5e and S6) and found that the heterolytic dissociation of H_2 at the Ce-O site to produce hydride species is kinetically the most favorable one. The energy barrier of this process is 0.47 eV, which is even lower than the corresponding energy barrier on the Cu/CeO_2 surface (0.56 eV). This result further indicates the great ability of the $Cu/CeO_2(111)$ in generating surface hydride species.

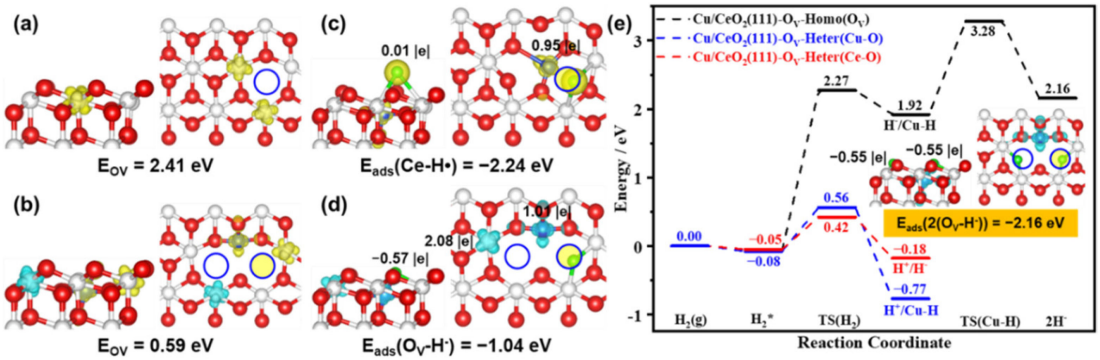

Figure 5. Calculated structures (left: side view; right: top view) of the (**a**) reduced CeO_2(111) with one surface oxygen vacancy and (**b**) reduced Cu/CeO_2(111) with one inherent surface oxygen vacancy and an extra surface oxygen vacancy. Calculated structures (left: side view; right: top view) of a single H at the oxygen vacancy sites of the (**c**) Cu/CeO_2(111) and (**d**) reduced Cu/CeO_2(111)-O_V surfaces. (**e**) Calculated energy profiles of homolytic (Homo) and heterolytic (Heter) H_2 dissociation on the Cu/CeO_2(111)-O_V surface. The unfilled blue circle represents the surface oxygen vacancy, and the blue circle filled with yellow represents the inherent surface oxygen vacancy on the Cu/CeO_2(111). The spin density distributions are illustrated in yellow and blue, and the surface oxygen vacancy formation energies are also given.

3.4. Selective Hydrogenation of CO_2

To unveil the catalytic activities of the various surfaces, we then continued to study the main reaction steps of the CO_2RR at CeO_2(111) and Cu/CeO_2(111) (Figures 6, S7 and S8). It is generally accepted that the adsorption and activation of CO_2 and the generation of hydride species are the key steps of the whole CO_2RR [10,11,38]. As shown in Figure 6, the adsorption of CO_2 on the Cu/CeO_2(111) surface is exothermic by 1.06 eV. In comparison, the adsorption of CO_2 on the CeO_2(111) surface is much weaker, with an exothermic adsorption energy of 0.32 eV only. Therefore, the Cu dopant can indeed promote CO_2 adsorption. This is mainly attributed to the relatively high energy level of the occupied Cu 3*d* orbital which can donate its electron to the CO_2 molecule (Figure 1d). This is also consistent with some previous experimental observation [13]. Then we calculated the adsorption of H_2 and found that the adsorption of H_2 is weak on both the CeO_2(111) and Cu/CeO_2(111) surfaces with pre-adsorbed CO_2, and the corresponding adsorption energies are 0.01 and 0.12 eV, respectively, which are largely close to those on the clean surfaces (Figure 3). Nevertheless, since the adsorption of CO_2 is stronger than that of H_2 on both the CeO_2(111) and Cu/CeO_2(111) surfaces, it is reasonable to consider the dissociative adsorption of H_2 on the CO_2 pre-covered surfaces.

Since our calculated results presented above already showed that the hydride species are kinetically and thermodynamically unstable at CeO_2(111), we only considered the formation of two hydroxyl species on the CO_2 pre-adsorbed CeO_2(111) through H_2 dissociation. This process needs to overcome a barrier of 0.83 eV and is exothermic by 2.67 eV (Figure 6). We found that the produced proton species has rather low activities in the hydrogenation of CO_2 to HCOO* or COOH*, with the calculated barriers being higher than 3 eV. Moreover, the COOH pathway is both thermodynamically and kinetically more favorable than the HCOO pathway on this surface.

By contrast, on the Cu/CeO_2(111) surface, hydride species can be stable, and H_2 can readily dissociate into one hydride and one OH^- species. This process needs to overcome a barrier of 0.79 eV and is exothermic by 0.55 eV. We found that the produced hydride species is quite active for CO_2 hydrogenation. In the HCOO pathway, the calculated barrier and reaction energy are 1.20 and 0.18 eV, respectively, while in the COOH pathway, the corresponding values are 1.34 and −1.59 eV, respectively. Although the generated COOH* species is more stable than the HCOO* species, the HCOO pathway is kinetically more favorable than the COOH pathway. We also studied the reaction of CO_2 hydrogenation by

H^+ to form COOH* on the $Cu/CeO_2(111)$ surface, and the calculated barrier is extremely high (4.47 eV). These results indicate that the as-formed hydride species is crucial to the activity and selectivity of the $Cu/CeO_2(111)$ in the CO_2 reduction reaction.

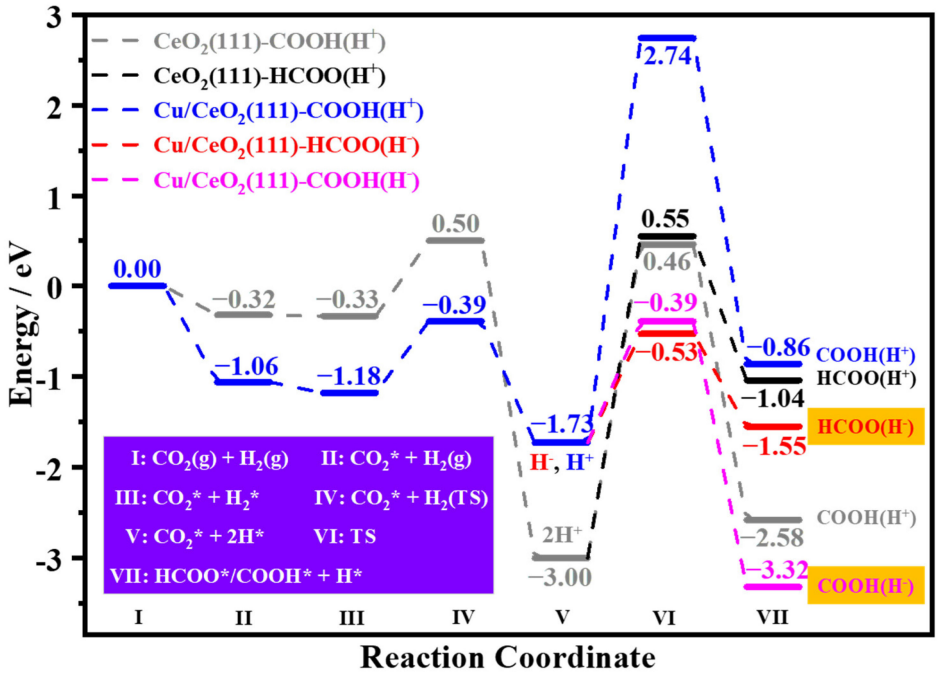

Figure 6. Calculated energy profiles of the first few key steps of the CO_2 hydrogenation reaction on the $CeO_2(111)$ and $Cu/CeO_2(111)$ surfaces.

4. Conclusions

In conclusion, we systematically studied the hydride formation and its reaction with CO_2 on the pristine and Cu-doped $CeO_2(111)$ surfaces. The calculated results showed that the hydride species are thermodynamically and kinetically unstable on the pristine $CeO_2(111)$ surface, and the adsorption of CO_2 on this surface is rather weak. In contrast, kinetically stable hydride species can be effectively produced by heterolytic H_2 dissociation on the $Cu/CeO_2(111)$ surface with inherent oxygen vacancies. We also found that the Cu dopant promotes the formation of oxygen vacancies, which is favorable for the generation of hydride species. Moreover, the Cu dopant also promotes the adsorption of CO_2, and the hydrogenation of CO_2 to HCOO* can be significantly facilitated by the hydride species on the $Cu/CeO_2(111)$ surface, showing that the doping of Cu significantly improves the activity and selectivity of the $CeO_2(111)$ toward the hydrogenation of CO_2 to methanol. Our findings may guide the rational design of efficient ceria and Cu based catalysts for CO_2 reduction reactions.

Supplementary Materials: The following are available online at https://www.mdpi.com/article/10.3390/catal12090963/s1, Tables S1 and S2: Calculated lattice constants of bulk ceria by using different plane wave kinetic energy cutoff and different *k*-point mesh densities. Table S3: Calculated Bader charges of the Cu^{2+} of CuO and the Cu^{1+} of Cu_2O. Table S4: Calculated Bader charges of the Cu and Ce species and their nearby O; calculated Cu-O and Ce-O bond distances, and the electrostatic interaction energies (E_{Cu+Ce}) between the Cu and Ce and their nearby species on the $Cu/CeO_2(111)$ and the $Cu/CeO_2(111)$ surface with H being adsorbed at the O site; calculated Cu coordinate numbers on the $Cu/CeO_2(111)$ and the $Cu/CeO_2(111)$ surface with H being adsorbed at the O site. Figure S1: Calculated density of states (DOS) of the $Cu/CeO_2(111)$ surface with H being adsorbed at the Cu site. Figure S2: Calculated structures of $Cu/CeO_2(111)$ and $Cu/CeO_2(111)$ with adsorbed H which gives to the localized electron at different site. Figure S3: Calculated density of states (DOS) of the $Cu/CeO_2(111)$ surface with H being adsorbed at the O site. Figure S4: Calculated structures

of H_2 adsorption and dissociation on the CeO_2(111) surface. Figure S5: Calculated structures of H_2 adsorption and dissociation on the Cu/CeO_2(111) surface. Figure S6: Calculated structures of H_2 adsorption and dissociation on the Cu/CeO_2(111)-O_V surface. Crystal Reduction Potential (Vr). Figure S7: Calculated structures of CO_2 hydrogenation on the CeO_2(111) surface. Figure S8: Calculated structures of CO_2 hydrogenation on the Cu/CeO_2(111) surface. References [27,38,57] are cited in the Supplementary Materials.

Author Contributions: Conceptualization, X.-P.W. and X.-Q.G.; methodology, H.-H.L. and Z.-Q.W.; software, H.-H.L. and Z.-Q.W.; validation, Z.-Q.W.; formal analysis, Z.-Q.W., X.-P.W. and X.-Q.G.; investigation, Z.-Q.W.; resources, X.-Q.G.; data curation, H.-H.L. and Z.-Q.W.; writing—original draft preparation, Z.-Q.W.; writing—review and editing, X.-P.W. and X.-Q.G.; visualization, Z.-Q.W.; supervision, X.-P.W., P.H. and X.-Q.G.; project administration, X.-Q.G.; funding acquisition, X.-P.W., P.H. and X.-Q.G. All authors have read and agreed to the published version of the manuscript.

Funding: This research was funded by National Key R&D Program of China (2018YFA0208602) and National Nature Science Foundation of China (21825301, 22003016, 92045303, 92145302) and Shanghai Sailing Program (21YF1409400) and China Postdoctoral Science Foundation (2020M671020).

Data Availability Statement: Not applicable.

Conflicts of Interest: The authors declare no conflict of interest.

References

1. Gianvito, V.; Patrick, D.; Julia, V.; Miguel, B.; Sebastián, C.; Mónica, C.; Adrian, B.; Javier, P.-R. Promoted Ceria Catalysts for Alkyne Semi-hydrogenation. *J. Catal.* **2015**, *324*, 69–78.
2. Esrafilzadeh, D.; Zavabeti, A.; Jalili, R.; Atkin, P.; Choi, J.; Carey, B.J.; Brkljača, R.; O'Mullane, A.P.; Dickey, M.D.; Officer, D.L.; et al. Room Temperature CO_2 Reduction to Solid Carbon Species on Liquid Metals Featuring Atomically Thin Ceria Interfaces. *Nat. Commun.* **2019**, *10*, 865. [CrossRef]
3. Rodriguez, J.A.; Grinter, D.C.; Liu, Z.; Palomino, R.M.; Senanayake, S.D. Ceria-based Model Catalysts: Fundamental Studies on the Importance of the Metal—Ceria Interface in CO Oxidation, the Water—Gas Shift, CO_2 Hydrogenation, and Methane and Alcohol Reforming. *Chem. Soc. Rev.* **2017**, *46*, 1824–1841. [CrossRef] [PubMed]
4. Vilé, G.; Bridier, B.; Wichert, J.; Pérez-Ramírez, J. Ceria in Hydrogenation Catalysis: High Selectivity in the Conversion of Alkynes to Olefins. *Angew. Chem. Int. Ed.* **2012**, *51*, 8620–8623. [CrossRef] [PubMed]
5. Riley, C.; Zhou, S.; Kunwar, D.; Riva, A.D.L.; Peterson, E.; Payne, R.; Gao, L.; Lin, S.; Guo, H.; Datye, A. Design of Effective Catalysts for Selective Alkyne Hydrogenation by Doping of Ceria with a Single-atom Promotor. *J. Am. Chem. Soc.* **2018**, *140*, 12964–12973. [CrossRef]
6. James, K.; Jisue, M.; Wu, Z.L. A Review of the Interactions between Ceria and H_2 and the Applications to Selective Hydrogenation of Alkynes. *Chin. J. Catal.* **2020**, *41*, 901–914.
7. Wang, F.; Wei, M.; Evans, D.G.; Duan, X. CeO_2-based Heterogeneous Catalysts toward Catalytic Conversion of CO_2. *J. Mater. Chem. A* **2016**, *4*, 5773–5783. [CrossRef]
8. Chang, K.; Zhang, H.C.; Cheng, M.-J.; Lu, Q. Application of Ceria in CO_2 Conversion Catalysis. *ACS Catal.* **2020**, *10*, 613–631. [CrossRef]
9. Jiang, F.; Wang, S.S.; Liu, B.; Liu, J.; Wang, L.; Xiao, Y.; Xu, Y.B.; Liu, X.H. Insights into the Influence of CeO_2 Crystal Facet on CO_2 Hydrogenation to Methanol over Pd/CeO_2 Catalysts. *ACS Catal.* **2020**, *10*, 11493–11509. [CrossRef]
10. Cheng, Z.; Lo, C.S. Mechanistic and Microkinetic Analysis of CO_2 Hydrogenation on Ceria. *Phys. Chem. Chem. Phys.* **2016**, *18*, 7987–7996. [CrossRef] [PubMed]
11. Kumari, N.; Haider, M.A.; Agarwal, M.; Sinha, N.; Basu, S. Role of Reduced CeO_2 Surface for CO_2 Reduction to CO and Methanol. *J. Phys. Chem. C* **2016**, *120*, 16626–16635. [CrossRef]
12. Zhang, W.; Ma, X.-L.; Xiao, H.; Lei, M.; Li, J. Mechanistic Investigations on Thermal Hydrogenation of CO_2 to Methanol by Nanostructured CeO_2: The Crystal-Plane Effect on Catalytic Reactivity. *J. Phys. Chem. C* **2019**, *123*, 11763–11771. [CrossRef]
13. Zhao, Y.-F.; Yang, Y.; Mims, C.; Peden, C.H.F.; Li, J.; Mei, D.H. Insight into Methanol Synthesis from CO_2 Hydrogenation on Cu(111): Complex Reaction Network and the Effects of H_2O. *J. Catal.* **2011**, *281*, 199–211. [CrossRef]
14. Kuld, S.; Thorhauge, M.; Falsig, H.; Elkjær, C.F.; Helveg, S.; Chorkendorff, I.; Sehested, J. Quantifying the Promotion of Cu Catalysts by ZnO for Methanol Synthesis. *Science* **2016**, *352*, 969–974. [CrossRef] [PubMed]
15. Kattel, S.; Ramırez, P.J.; Chen, J.G.; Rodriguez, J.A.; Liu, P. Active Sites for CO_2 Hydrogenation to Methanol on Cu/ZnO Catalysts. *Science* **2017**, *355*, 1296–1299. [CrossRef]
16. Liu, S.P.; Zhao, M.; Gao, W.; Jiang, Q.; Jacob, T. Theoretical Studies on the CO_2 Reduction to CH_3OH on Cu(211). *Electrocatalysis* **2017**, *8*, 647–656. [CrossRef]
17. Xu, D.; Ding, M.Y.; Hong, X.L.; Liu, G.L. Mechanistic Aspects of the Role of K Promotion on Cu−Fe-based Catalysts for Higher Alcohol Synthesis from CO_2 Hydrogenation. *ACS Catal.* **2020**, *10*, 14516–14526. [CrossRef]

18. Xu, D.; Wang, Y.Q.; Ding, M.Y.; Hong, X.L.; Liu, G.L.; Tsang, S.C.E. Advances in Higher Alcohol Synthesis from CO_2 Hydrogenation. *Chem* **2020**, *7*, 849–881. [CrossRef]
19. Liu, H.X.; Li, S.Q.; Wang, W.W.; Yu, W.-Z.; Zhang, W.-J.; Ma, C.; Jia, C.-J. Partially Sintered Copper–Ceria as Excellent Catalyst for the High-Temperature Reverse Water Gas Shift Reaction. *Nat. Commun.* **2022**, *13*, 867. [CrossRef] [PubMed]
20. Wang, B.B.; Zhang, L.J.; Cai, J.; Peng, Z.; Cheng, P.H.; Li, X.B.; Zhang, H.; Yang, F.; Liu, Z. Formation and Activity Enhancement of Surface Hydrides by the Metal–Oxide Interface. *Adv. Mater. Interfaces* **2021**, *8*, 2002169. [CrossRef]
21. Wang, S.; Zheng, M.H.; Li, M.; Wu, X.J.; Xia, C.R. Synergistic Effects towards H_2 Oxidation on the Cu–CeO_2 Electrode: A Combination Study with DFT Calculations and Experiments. *J. Mater. Chem. A* **2016**, *4*, 5745–5754. [CrossRef]
22. Wan, Q.; Wei, F.F.; Wang, Y.Q.; Wang, F.T.; Zhou, L.S.; Lin, S.; Xie, D.Q.; Guo, H. Single Atom Detachment from Cu Clusters, and Diffusion and Trapping on CeO_2: Implications in Ostwald Ripening and Atomic Redispersion. *Nanoscale* **2018**, *10*, 17893–17901. [CrossRef] [PubMed]
23. Wang, Y.F.; Chen, Z.; Han, P.; Du, Y.H.; Gu, Z.X.; Xu, X.; Zheng, Z.F. Single-Atomic Cu with Multiple Oxygen Vacancies on Ceria for Electrocatalytic CO_2 Reduction to CH_4. *ACS Catal.* **2018**, *8*, 7113–7119. [CrossRef]
24. Yang, T.; Mao, X.N.; Zhang, Y.; Wu, X.P.; Wang, L.; Chu, M.Y.; Pao, C.-W.; Yang, S.Z.; Xu, Y.; Huang, X.Q. Coordination Tailoring of Cu Single Sites on C_3N_4 Realizes Selective CO_2 Hydrogenation at Low Temperature. *Nat. Commun.* **2021**, *12*, 6022. [CrossRef] [PubMed]
25. Schweke, D.; Shelly, L.; David, R.B.; Danon, A.; Kostirya, N.; Hayun, S. Comprehensive Study of the Ceria H_2 System: Effect of the Reaction Conditions on the Reduction Extent and Intermediates. *J. Phys. Chem. C* **2020**, *124*, 6180–6187. [CrossRef]
26. Fernandez-Torre, D.; Carrasco, J.; Ganduglia-Pirovano, M.V.; Perez, R. Hydrogen Activation, Diffusion, and Clustering on CeO_2: A DFT + U Study. *J. Chem. Phys.* **2014**, *141*, 014703. [CrossRef] [PubMed]
27. García-Melchor, M.; López, N. Homolytic Products from Heterolytic Paths in H_2 Dissociation on Metal Oxides: The Example of CeO_2. *J. Phys. Chem. C* **2014**, *118*, 10921–10926. [CrossRef]
28. Duchoň, T.; Hackl, J.; Mueller, D.N.; Kullgren, J.; Du, D.; Senanayake, S.D.; Mouls, C.; Gottlob, D.; Khan, M.M.I.; Cramm, S.; et al. Establishing Structure-sensitivity of Ceria Reducibility: Real-time Observations of Surface-hydrogen Interactions. *J. Mater. Chem. A* **2020**, *8*, 5501–5507. [CrossRef]
29. Vilé, G.; Colussi, S.; Krumeich, F.; Trovarelli, A.; Pérez-Ramírez, J. Opposite Face Sensitivity of CeO_2 in Hydrogenation and Oxidation Catalysis. *Angew. Chem. Int. Ed.* **2014**, *53*, 12069–12072. [CrossRef] [PubMed]
30. Wu, X.-P.; Gong, X.-Q.; Lu, G. Role of Oxygen Vacancies in the Surface Evolution of H at CeO_2: A Charge Modification Effect. *Phys. Chem. Chem. Phys.* **2015**, *17*, 3544–3549. [CrossRef]
31. Li, Z.; Werner, K.; Qian, K.; You, R.; Płucienik, A.; Jia, A.; Wu, L.; Zhang, L.; Pan, H.; Kuhlenbeck, H.; et al. Oxidation of Reduced Ceria by Incorporation of Hydrogen. *Angew. Chem. Int. Ed.* **2019**, *131*, 14828–14835. [CrossRef]
32. Wu, Z.; Cheng, Y.; Tao, F.; Daemen, L.; Foo, G.S.; Nguyen, L.; Zhang, X.; Beste, A.; Ramirez-Cuesta, A.J. Direct Neutron Spectroscopy Observation of Cerium Hydride Species on a Cerium Oxide Catalyst. *J. Am. Chem. Soc.* **2017**, *139*, 9721–9727. [CrossRef] [PubMed]
33. Werner, K.; Weng, X.; Calaza, F.; Sterrer, M.; Kropp, T.; Paier, J.; Sauer, J.; Wilde, M.; Fukutani, K.; Shaikhutdinov, S.; et al. Toward an Understanding of Selective Alkyne Hydrogenation on Ceria: On the Impact of O Vacancies on H_2 Interaction with CeO_2. *J. Am. Chem. Soc.* **2017**, *139*, 17608–17616. [CrossRef] [PubMed]
34. Coperet, C.; Estes, D.P.; Larmier, K.; Searles, K. Isolated Surface Hydrides: Formation, Structure, and Reactivity. *Chem. Rev.* **2016**, *116*, 8463–8505. [CrossRef]
35. Moon, J.; Cheng, Y.; Daemen, L.L.; Li, M.; Polo-Garzon, F.; Ramirez-Cuesta, A.J.; Wu, Z. Discriminating the Role of Surface Hydride and Hydroxyl for Acetylene Semi-Hydrogenation over Ceria through in Situ Neutron and Infrared Spectroscopy. *ACS Catal.* **2020**, *10*, 5278–5287. [CrossRef]
36. Wang, Q.R.; Guo, J.P.; Chen, P. The Power of Hydrides. *Joule* **2020**, *4*, 705–709. [CrossRef]
37. Li, Z.R.; Kristin, W.; Chen, L.; Jia, A.P.; Qian, K.; Zhong, J.Q.; You, R.; Wu, L.H.; Zhang, L.Y.; Pan, H.B.; et al. Interaction of Hydrogen with Ceria: Hydroxylation, Reduction, and Hydride Formation on the Surface and in the Bulk. *Chem. Eur. J.* **2021**, *27*, 5268–5276. [CrossRef]
38. Wang, Z.-Q.; Chu, D.-R.; Zhou, H.; Wu, X.-P.; Gong, X.-Q. Role of Low-Coordinated Ce in Hydride Formation and Selective Hydrogenation Reactions on CeO_2 Surfaces. *ACS Catal.* **2022**, *12*, 624–632. [CrossRef]
39. Kresse, G.; Furthmüller, J. Efficient Iterative Schemes for Ab Initio Total–Energy Calculations Using a Pane–Wave Basis Set. *Phys. Rev. B* **1996**, *54*, 11169–11186. [CrossRef]
40. Blöchl, P.E. Projector Augmented–wave Method. *Phys. Rev. B* **1994**, *50*, 17953–17979. [CrossRef]
41. Perdew, J.P.; Burke, J.; Ernzerhof, M. Generalized Gradient Approximation Made Simple. *Phys. Rev. Lett.* **1996**, *77*, 3865–3868. [CrossRef] [PubMed]
42. Teter, M.P.; Payne, M.C.; Allan, D.C. Solution of Schrodinger's Equation for Large Systems. *Phys. Rev. B* **1989**, *40*, 12255–12263. [CrossRef] [PubMed]
43. Kümmerle, E.; Heger, G. The Structures of C–$Ce_2O_{3+\delta}$, Ce_7O_{12}, and $Ce_{11}O_{20}$. *J. Solid State Chem.* **1999**, *147*, 485–500. [CrossRef]
44. Jerratsch, J.-F.; Shao, X.; Nilius, N.; Freund, H.-J.; Popa, C.; Ganduglia-Pirovano, M.V.; Burow, A.M.; Sauer, J. Electron Localization in Defective Ceria Films: A Study with Scanning-Tunneling Microscopy and Density-Functional Theory. *Phys. Rev. Lett.* **2011**, *106*, 246801. [CrossRef] [PubMed]

45. Nolan, M.; Parker, S.C.; Watson, G.W. The Electronic Structure of Oxygen Vacancy Defects at the Low Index Surfaces of Ceria. *Surf. Sci.* **2005**, *595*, 223–232. [CrossRef]
46. Nolan, M.; Grigoleit, S.; Sayle, D.C.; Parker, S.C.; Watson, G.W. Density Functional Theory Studies of the Structure and Electronic Structure of Pure and Defective Low Index Surfaces of Ceria. *Surf. Sci.* **2005**, *576*, 217–229. [CrossRef]
47. Vicario, G.; Balducci, G.; Fabris, S.; Gironcoli, S.D.; Baroni, S. Interaction of Hydrogen with Cerium Oxide Surfaces: A Quantum Mechanical Computational Study. *J. Phys. Chem. B* **2006**, *110*, 19380–19385. [CrossRef]
48. Michaelides, A.; Liu, Z.P.; Zhang, C.J.; Alavi, A.; King, D.A.; Hu, P. Identification of General Linear Relationships between Activation Energies and Enthalpy Changes for Dissociation Reactions at Surfaces. *J. Am. Chem. Soc.* **2003**, *125*, 3704–3705. [CrossRef]
49. Alavi, A.; Hu, P.; Deutsch, T.; Silvestrelli, P.L.; Hutter, J. CO Oxidation on Pt(111): An Ab Initio Density Functional Theory Study. *Phys. Rev. Lett.* **1998**, *80*, 3650–3653. [CrossRef]
50. Liu, Z.P.; Hu, P. General Rules for Predicting Where a Catalytic Reaction Should Occur on Metal Surfaces: A Density Functional Theory Study of C–H and C–O Bond Breaking/making on Flat, Stepped, and Kinked Metal Surfaces. *J. Am. Chem. Soc.* **2003**, *125*, 1958–1967. [CrossRef]
51. Somorjai, G.A.; Li, Y.M. *Introduction to Surface Chemistry and Catalysis*; Wiley-VCH: Berkeley, CA, USA, 2010.
52. Yang, Z.X.; He, B.L.; Lu, Z.S.; Hermansson, K. Physisorbed, Chemisorbed, and Oxidized CO on Highly Active Cu−CeO_2. *J. Phys. Chem. C* **2010**, *114*, 4486–4494. [CrossRef]
53. Zhou, S.L.; Wan, Q.; Lin, S. Cu/O Frustrated Lewis Pairs on Cu Doped CeO_2 for Acetylene Hydrogenation: A First-Principles Study. *Catalysts* **2022**, *12*, 74. [CrossRef]
54. Guo, C.; Wei, S.; Zhou, S.; Zhang, T.; Wang, Z.; Ng, S.-P.; Lu, X.; Wu, C.-M.L.; Guo, W. Initial Reduction of CO_2 on Pd-, Ru-, and Cu-Doped CeO_2 Surfaces: Effects of Surface Modification on Catalytic Activity and Selectivity. *ACS Appl. Mater. Interfaces* **2017**, *9*, 26107–26117. [CrossRef] [PubMed]
55. Wang, X.Q.; Rodriguez, J.A.; Hanson, J.C.; Gamarra, D.; Martínez-Arias, A.; Fernández-García, A. Unusual Physical and Chemical Properties of Cu in $Ce_{1-x}Cu_xO_2$ Oxides. *J. Phys. Chem. B* **2005**, *109*, 19595–19603. [CrossRef]
56. Wang, Z.-Q.; Wang, D.; Gong, X.-Q. Strategies to Improve the Activity while Maintaining the Selectivity of Oxidative Coupling of Methane at La_2O_3: A Density Functional Theory Study. *ACS Catal.* **2020**, *10*, 586–594. [CrossRef]
57. Wexler, R.B.; Gautam, G.S.; Stechel, E.B.; Carter, E.A. Factors Governing Oxygen Vacancy Formation in Oxide Perovskites. *J. Am. Chem. Soc.* **2021**, *143*, 13212–13227. [CrossRef]